Geophysical Prospecting

EAGE EUROPEAN ASSOCIATION OF GEOSCIENTISTS & ENGINEERS

Geophysical Prospecting, 2015 doi: 10.1111/1365-2478.12226

Converted-wave beam migration with sparse sources or receivers

Lorenzo Casasanta* and Samuel H. Gray

CGG, 715 5th Avenue SW, Calgary,, AB T2P 5A2 Canada

Received April 2014, revision accepted October 2014

ABSTRACT

Gaussian beam depth migration overcomes the single-wavefront limitation of most implementations of Kirchhoff migration and provides a cost-effective alternative to full-wavefield imaging methods such as reverse-time migration. Common-offset beam migration was originally derived to exploit symmetries available in marine towed-streamer acquisition. However, sparse acquisition geometries, such as cross-spread and ocean bottom, do not easily accommodate requirements for common-offset, common-azimuth (or common-offset-vector) migration. Seismic data interpolation or regularization can be used to mitigate this problem by forming well-populated common-offset-vector volumes. This procedure is computationally intensive and can, in the case of converted-wave imaging with sparse receivers, compromise the final image resolution. As an alternative, we introduce a common-shot (or common-receiver) beam migration implementation, which allows migration of datasets rich in azimuth, without any regularization pre-processing required. Using analytic, synthetic, and field data examples, we demonstrate that converted-wave imaging of ocean-bottom-node data benefits from this formulation, particularly in the shallow subsurface where regularization for common-offset-vector migration is both necessary and difficult.

Key words: Anisotropy, Imaging, Multicomponent.

INTRODUCTION

The Earth is an elastic medium and seismic energy propagates inside the Earth in the form of elastic waves. Most seismic acquisition and processing methods assume that seismic wavefields consist entirely of compressional (P) waves or, effectively, that the Earth is an acoustic medium. This assumption has been proven useful, especially in the imaging of structural targets. For purposes of lithology discrimination, however, and sometimes even for structural purposes, the limitations of P-wave seismic data processing are well known (Stewart *et al.* 2003). For example, lithology discrimination in unconventional reservoirs such as shales is typically more accurate when conventional P-wave processing is combined with converted-wave (C- or PS-wave) processing, which uses recorded shear (S-wave) energy generated from P-wave sources. Also, seismic images of geologic structures beneath gas clouds using PS-wave data are often better than images obtained from P-wave data.

Elastic migration uses an elastic wave equation to downward continue and image elastic waves inside the Earth. PS imaging is a specialization of elastic imaging using P- and S-wave equations to downward continue wavefields from source and receiver locations, respectively. In both downward continuation and imaging steps, PS migration normally assumes that conversion from P- to S-wave occurs only at reflector locations (Stewart *et al.* 2002) and that S-waves are vertically polarized. These assumptions allow complete decoupling of P- and S-wavefields, a considerable gain in algorithmic simplicity and computational efficiency. These gains come with some costs. One is the effect of mishandling many possible reflection events for which conversion from P- to S-wave (or vice versa) has occurred during transmission. A second comes from the incomplete separation of recorded wavefields from vertical and horizontal particle motion into P- and S-components. Each of these can contribute a significant amount of noise to

*E-mail: lorenzo.casasanta@cgg.com

the migrated image, and their net effect can degrade image quality to a level well below that of the conventional P-wave image. In spite of this, the use of PS processing, and imaging in particular, is increasing.

Most PS imaging is performed using Kirchhoff migration (Kuo and Dai 1984; Hokstad 2000) in time or depth, generalized Radon transform (GRT) migration (Burridge *et al.* 1998; Ursin 2004; Koren and Ravve 2011; Ravve and Koren 2011), or reverse-time migration (RTM; Sun and McMechan 2001). Kirchhoff migration remains the workhorse, mostly for reasons of flexibility and computational efficiency. These approaches are based on elastic theory, but they are usually specialized to PS imaging of decoupled downgoing P- and upgoing S-wavefields.

For PS depth migration, both standard Kirchhoff migration and RTM have significant problems. Standard Kirchhoff migration, in which rays are traced from source and receiver locations, works well for anisotropic P-wave imaging in areas of moderate structural complexity with moderate lateal P-wave velocity variations. For PS migration, the presence of anisotropy affects S-wave travel times more than it affects P-wave travel times: (i) even homogeneous media can produce S-wave triplications (but not P-wave triplications), with associated multivalued travel times, in the presence of strong anisotropy; (ii) a percentage velocity change due to a given anisotropy value will produce greater travel-time changes from low S-wave velocities than from high P-wave velocities. Further, interpolating S-wave travel times from a cone of ray paths on to a single-valued table on the migration grid causes greater travel-time discontinuities than for P-wave migration, leading to a high level of PS migration noise. We emphasize that the noisy character of standard Kirchhoff-migrated images (both P- and PS-wave) is due more to the discontinuities in single-valued travel-time tables than to inaccuracies in ray tracing, which nevertheless limit the accuracy of images produced by nonstandard Kirchhoff and beam migrations.

For RTM, there are two significant problems, namely, the first computational and the second algorithmic. The computational problem is caused by the range of velocities present in P-wave and S-wave velocity models. The computational grid spacing for RTM requires a certain number of points per wavelength, and extremely low velocities in the S-wave velocity model (on the order of 100 m/s at water bottom in some areas) imposes a very fine computational grid in all spatial dimensions. (Kirchhoff migration has the same problem in principle, but workarounds based on migration anti-aliasing loosen the grid spacing requirements.) The algorithmic problem is caused by S-wave anisotropy. Anisotropic PS RTM uses an "acoustic" (i.e., single-mode) approximation (e.g., Alkhalifah 2000) to propagate P-waves and S-waves separately in transversely isotropic media. This equation can be adapted to media where the symmetry axis of anisotropy is not vertical (tilted transverse isotropy or TTI) (Fowler, Du, and Fletcher 2010; Zhang, Zhang, and Zhang 2009) and to lower symmetry order such as orthorhombic anisotropy (Fowler and King 2011; Zhang and Zhang 2011), but for S-wave propagation, Finite difference implementations are conveniently applied only to weakly anisotropic media (Thomsen 1986) with limited accuracy in areas of strong anisotropy.

Another problem for both Kirchhoff migration and RTM is the handling of polarity of data recorded by horizontally polarized geophones. In processing, this manifests itself most obviously as a polarity reversal at small source–receiver offsets, which is usually compensated by applying a radial/transverse projection of the unmigrated horizontally polarized data and retaining the radial component. In 2D, this corresponds to polarity reversal in the unmigrated data for either positive or negative offsets. Often, the actual polarity reversal (more correctly, transition from positive to negative polarity) occurs at a nonzero offset (Rosales and Rickett 2001), and the applied p sign reversal causes an incorrect polarity for a range of traces, leading to cancellation errors in the migration operator. To overcome this problem, polarity, which is due to the direction of recorded particle motion in the upgoing S-wavefield, should be tracked into the subsurface using knowledge of P- and S-wave polarizations; this is difficult for both standard Kirchhoff migration and RTM.

In this paper we propose PS beam migration as an alternative to Kirchhoff, GRT, and RTMs. Gaussian beam migration (GBM) (Hill 2001; Gray 2005) and GRT migration can be applied to PS imaging with at least partial solutions to problems aforementioned. For both beam and GRT migrations: (i) the ability to handle multiple arrivals overcomes the most significant problem of standard Kirchhoff migration (although wavefield inaccuracy caused by ray tracing remains); (ii) the fine grid spacing requirements of RTM can be relaxed as for Kirchhoff migration; (iii) treatment of strong S-wave anisotropy can be handled as in Kirchhoff migration ray tracing; and (iv) S-wavefield polarization can be tracked into the subsurface to a good approximation. Our choice of beam migration is based on its use of local slant stacks of the unmigrated records, related to wavefield directions at the source or recording surface; these provide an efficiency advantage over GRT migration.

In addition to problems already mentioned, PS-wave data acquired on the seafloor present challenges to all migration

methods. At shallow depths, even for horizontal reflectors, reflection points do not lie below source–receiver midpoints, and narrow S-wave illumination cones prevent complete imaging. Sparsely sampled sources or receivers cause migration operator aliasing problems that need careful attention. Sparse sampling also complicates the decision, for ray-based migrations, to use common-shot, common-receiver, or common-offset-vector (COV) data volumes for optimal near-surface imaging. COV volumes, in particular, pose a number of problems for PS beam migration of seafloor data.

One of our goals is to describe practical solutions to all these issues provided by beam migration and to illustrate these solutions on synthetic and field PS-wave data. The second goal is to describe, in particular, how GBM handles pathological multipathing that can occur in PS-wave propagation. To accomplish these goals, we develop PS beam migration algorithms that can be applied to data volumes with sparsely sampled sources or receivers, i.e., seafloor recording with widely spaced node receivers (ocean-bottom node (OBN)) or widely spaced cables (ocean-bottom cable (OBC)) and relatively fine source spacing. We present two versions of PS beam migration of seafloor data: migration of COV volumes (Cary 1999) and migration of common-receiver volumes. In both versions we discuss theoretical and practical challenges, which arise mostly from poor data sampling. We next describe S-wave modeling in anisotropic media and point out associated difficulties for finite-difference wavefield extrapolators used in RTM. We then use analytic examples to illustrate the relative performance of alternative formulations of common-receiver PS GBM in the presence of strong multipathing. Finally, we use synthetic and real examples to illustrate (i) the advantages of PS beam migration over Kirchhoff migration and (ii) the relative performance of COV and common-receiver beam migrations, especially for near-surface imaging from sparse receiver locations.

COMMON-OFFSET-VECTOR AND COMMON-RECEIVER PS BEAM MIGRATIONS

Common-offset-vector migration and associated data preparation issues

COV migration is the 3D generalization of 2D common-offset migration in which the unmigrated volumes contain traces which, in principle, all share the same (nominal) source–receiver lateral offset vector. COV migration has the advantage of producing migrated common image gathers (CIGs), indexed by the nominal offset vector of each COV volume, with no additional effort over migrating a set of COVs. For P-wave migration, these CIGs are useful for tomography. COV migration also has a disadvantage when receiver spacing is large. Then, the tiles making up the COV volumes (called offset-vector tiles or OVTs) become large (Li 2008), with a wide range of offsets and azimuths, but they are sparsely populated with traces. When this happens, seismic data interpolation and regularization can be used to form well-populated (i.e., single-fold) COV volumes, but (i) this procedure is least effective exactly where it is most needed, at shallow depths, and (ii) the variety of offsets and azimuths complicates evaluation of the slant stacks used in beam imaging. As a result, COV migrated stacks can be inaccurate, especially at shallow depths.

COV PS beam migration (Casasanta and Grion 2012) is, in principle, a straightforward extension of Hill's (2001) COV P-wave GBM. In practice, the presence of two different velocity fields (P and S) causes many implementation modifications. All traces in a COV volume are assumed to have the same lateral offset vector (i.e., offset and azimuth) between the source and the receiver, although elevations may be different with, for example, the source at or near the sea surface and the receiver at the seafloor. Gaussian beams provide Green's functions for P-wave propagation from source locations and S-wave propagation from receiver locations to image points. Adapting Hill's (2001) formula for migration of a single COV, with half-offset vector $\mathbf{h}$, to PS migration yields an expression for image $I_{\mathrm{h}}(\mathbf{x})$ at subsurface location $\mathbf{x}$:

$$I_{\mathrm{h}}(\mathbf{x}) \approx -C_0 \sum_{\mathbf{L}} \int d\omega \times \int\int dp_x^m dp_y^m U_{\mathrm{h}}^{PS}(\mathbf{x}, \mathbf{p}^s, \mathbf{p}^r; \mathbf{L}, \omega) D_{\mathrm{h}}(\mathbf{p}^m; \mathbf{L}, \omega). \quad (1)$$

In this expression, seismic data D_{h} are local slant-stacked radial traces with horizontal direction vectors $\mathbf{p}^m = \mathbf{p}^s + \mathbf{p}^r$ at beam centre positions $\mathbf{L}$ and temporal frequency ω, and coefficient C_0 is a constant related to the geometry of the lattice for beam centres $\mathbf{L}$. Operator U_{h}^{PS} describes PS depth mapping of a single directional component $\mathbf{p}^m$ of data D_{h}:

$$U_{\mathrm{h}}^{PS}(\mathbf{x}, \mathbf{p}^s, \mathbf{p}^r; \mathbf{L}, \omega) = -\frac{i\omega}{2\pi} \int\int \frac{dp_x^h dp_y^h}{p_z^s} A_{PS}^*(\mathbf{x}, \mathbf{p}^s, \mathbf{p}^r; \mathbf{L}) \times \exp\left[-i\omega T_{PS}^*(\mathbf{x}, \mathbf{p}^s, \mathbf{p}^r; \mathbf{L})\right], \quad (2)$$

where $A_{PS}(\mathbf{x}, \mathbf{p}^s, \mathbf{p}^r; \mathbf{L}) = A_P(\mathbf{x}, \mathbf{p}^s; \mathbf{s}) A_S(\mathbf{x}, \mathbf{p}^r; \mathbf{r})$ and $T_{PS}(\mathbf{x}, \mathbf{p}^s, \mathbf{p}^r; \mathbf{L}) = T_P(\mathbf{x}, \mathbf{p}^s; \mathbf{s}) + T_S(\mathbf{x}, \mathbf{p}^r; \mathbf{r})$ are the product and the sum of P-wave source-side ($\mathbf{s} = \mathbf{L} - \mathbf{h}$) and S-wave receiver-side ($\mathbf{r} = \mathbf{L} + \mathbf{h}$) Gaussian beam amplitudes and

complex travel times. Asterisk * denotes complex conjugate. These quantities are computed by Gaussian beam ray tracing (Hill 2001) modified for P- and S-wave anisotropy (Zhu, Gray, and Wang 2007). Hill (2001) has given prescriptions for forming slant stacks D_{h} and specifying beam centre locations **L**.

There is some latitude in the choice of directional spacings for beam migration. These spacings determine initial ray directions from source and receiver locations, and they also determine slant-stack directions for constructing data D_{h}. Following Hill (2001), we keep spacings Δp_x and Δp_y constant and equal; hence, they are identical for source and receiver sides. The direction vectors $\mathbf{p}^s$ and $\mathbf{p}^r$ have initial magnitudes $\sin\theta / V$ where θ is the ray incidence angle at a source location or the ray emergence angle at a receiver location, and $V = V_{P0}$ (P-wave velocity) at a source location and $V = V_{S0}$ (S-wave velocity) at a receiver location. Because V_{P0} and V_{S0} are usually very different from each other, the actual angular spacings we use from source and receiver sides are different from each other.

COV beam migration was originally developed for narrow-azimuth marine streamer P-wave surveys, and it can also be applied to adequately sampled wide-azimuth surveys. Streamer surveys, especially narrow-azimuth, normally have relatively fine spacing of sources and receivers, both inline (in the streamer direction) and crossline. Marine PS migration uses data from sensors placed on the seafloor, with relatively fine spacing of sources near the sea surface. Receiver spacing is usually much coarser than source spacing in at least one direction, for both OBC acquisition and OBN acquisition. In the former, receiver spacing along cables is relatively fine (typically tens of meters), and cable spacing can be fine or coarse. In the latter, receiver spacing along nodes is coarse, usually hundreds of meters. Coarse spatial sampling for both OBC (with large cable spacing) and OBN surveys presents severe imaging challenges to COV beam migration; we describe these next.

Calvert *et al.* (2008) describe the process of populating OVTs (Vermeer 2012) for land pre-stack migration. Each COV volume is built from a set of non-overlapping OVTs, with each OVT containing a single trace at each common-midpoint (CMP) location, i.e., single-fold. For orthogonal acquisition (source lines perpendicular to receiver lines), OVTs are rectangular, and their size is determined by source and receiver line spacings. If line spacings are large, then OVTs are large, with a large range of actual offset vectors within each OVT, resulting in significant deviation from the central offset and azimuth of the COV. This violates a requirement of COV beam migration that all traces in a COV volume have identical source–receiver offset vectors, and it leads to the need to regularize most, if not all, traces in each volume by differential normal-moveout (NMO) correction or some more advanced process. For OBC acquisition with fine inline and crossline source spacings, the source-line spacing makes OVTs smaller in one direction than for standard land orthogonal geometries. For OBN acquisition (Vermeer 2012), OVTs are again smaller in one direction, but large "inline" node separation causes the OVTs to be underpopulated. This, in turn, leads to the need to populate OVTs by some interpolation technique (e.g., Trad 2009), in addition to the need to regularize most of the originally acquired traces. Depending on the relative sizes of node spacing and CMP spacing, the amount of data created by interpolation can be enormous, with the number of interpolated traces outnumbering the number of acquired traces by an order of magnitude or more.

For data acquired with sources near the sea surface and receivers at the seafloor, there is an additional problem, namely, the difficulty of interpolating such data (Vermeer 2012). A regularization normally applied to the problem of seismic data interpolation of sparse data is the application of NMO to the acquired traces, which assumes that reflections occur at source–receiver midpoints. This assumption is violated for seafloor acquisition when sources are near the sea surface, and it is further egregiously violated for converted waves, where different P- and S-wave velocities cause reflections to occur away from midpoints, especially at shallow depths below the seafloor. Also, it is difficult to train PS interpolation to be sensitive to polarity without considering the simultaneous interpolation of all recorded components (radial, transverse, and vertical), a problem that potentially exceeds PS imaging in scope. Finally, extensive experimentation with interpolation techniques applied to sparse data has shown that, even for P-wave data, interpolation is least effective at shallow depths (near the seafloor, where it is most needed), where the methods benefit least from high fold.

Despite these difficulties, we developed and tested COV PS beam migration, and we show its superiority to Kirchhoff migration in the real data example.

Common-receiver migration

Alternatives to COV migration are common-shot and common-receiver migrations. Of the two, common-receiver migration is more attractive for seafloor data because (i) there are typically fewer receivers than shots and (ii) shot spacing is typically smaller than receiver spacing so that

common-receiver records are better-sampled wavefields than common-shot records and are less prone to aliasing before and during migration.

Common-receiver PS beam migration is, in principle, a straightforward extension of Gray's (2005) common-shot P-wave GBM, with fewer practical complications than for COV migration. Analogous to equation (1), the common-receiver GBM expression for image I_r (x) at subsurface location **x**, from a record with receiver location **r**, can be written as

$$I_{\mathrm{r}}(\mathbf{x}) \approx -C_0 \sum_{\mathrm{L}} \int d\omega \times \int\int dp_x^s dp_y^s U_{\mathrm{r}}^{PS}(\mathbf{x}, \mathbf{p}^s, \mathbf{p}^r; \mathbf{L}, \omega) D_{\mathrm{r}}(\mathbf{p}^s; \mathbf{L}, \omega); \quad (3)$$

$$U_{\mathrm{r}}^{PS}(\mathbf{x}, \mathbf{p}^s, \mathbf{p}^r; \mathbf{L}, \omega) = -\frac{i\omega}{2\pi} \int\int dp_x^r dp_y^r A_{PS}^*(\mathbf{x}, \mathbf{p}^s, \mathbf{p}^r; \mathbf{L}) \times \exp\left[-i\omega T_{PS}^*(\mathbf{x}, \mathbf{p}^s, \mathbf{p}^r; \mathbf{L})\right]. \quad (4)$$

Here, seismic data D_{r} are local slant-stacked traces with direction vectors $\mathbf{p}^s$ at beam centre positions **L**. The major differences between equations (1)–(2) and (3)–(4) are: (i) the slant stack is performed on COV data in equation (1) and on common-receiver data in equation (3); and (ii) integration variables are $\mathbf{p}^m$ and $\mathbf{p}^h$ in equations (1) and (2) and $\mathbf{p}^s$ and $\mathbf{p}^r$ in equations (3) and (4). An alternative formulation (Gray 2005) retains the first of these differences while eliminating the second. We describe the relative merits of these two versions later in our discussion of S-wave multipathing. When source spacing is fine, there is no need for the interpolation and regularization processes used to condition the data for COV slant stacking. However, coarse receiver spacing, especially for OBN data, will limit the ability of any migration method to image at shallow depths. At all depths, spatial sampling of sources and receivers presents a trade-off in resolution and accuracy between COV migration and common-receiver migration.

Spatial sampling and migration aliasing

Both COV migration and common-receiver migration are two-step processes: the first step is forming the slant stacks, and the second step is mapping the slant-stacked data in the subsurface. In both steps, care must be taken to avoid operator aliasing (Beasley and Mobley 1988), which is a function of the spatial sampling and maximum frequency of the data, and velocity at source or receiver locations (Vermeer 1990). For COV migration, the spatial sample rate is the CMP spacing, and slant stacking and mapping are both performed in the $\mathbf{p}^m = \mathbf{p}^s + \mathbf{p}^r$ domain; operator anti-aliasing requirements (using the CMP spacing) are the same for both slant stacking and mapping. For common-receiver migration, the spatial sample rate is the source spacing, and slant stacking is performed in the $\mathbf{p}^s$ domain, whereas mapping is performed in the $\mathbf{p}^r$ domain; therefore operator anti-aliasing requirements are different for slant stacking and mapping. Gray (2013) analysed operator anti-aliasing in general for pre-stack migration and concluded that a sufficient condition for complete anti-aliasing in common-receiver migration is to apply the more conservative of common-shot and common-receiver conditions, i.e., based on the larger of source and receiver spacings. This requires, in addition to anti-aliasing the slant stacking (using the source spacing), anti-aliasing the mapping (using the receiver spacing). With large receiver spacings typical of seafloor recording, applying such conservative anti-aliasing to the mapping will overly restrict the maximum frequencies used, resulting in a dramatic loss of resolution in the image (Gray 2013). For common-receiver migration, we typically apply some percentage, considerably less than 100%, of the theoretically complete anti-aliasing while mapping. This allows a certain amount of aliasing noise into a migrated image, but it retains good image resolution. In fact, as the OBN examples show, the shallow image from common-receiver migration can be more accurate than the corresponding image from COV migration, which suffers from smearing due to data interpolation.

Polarity correction while imaging

PS migration is normally performed on the horizontal component of data from receivers that detect particle motion, including direction. P-wave energy that reflects in the subsurface and converts to S-wave energy undergoes changes in particle motion direction. At a reflecting interface and in the plane of reflection, these changes are described by Sun and McMechan (2001, Appendix A). Typically, the polarity of recorded P–S data from an interface will change as a function of incidence angle, i.e., as incident P-wave polarization direction passes through normal incidence on the reflector. The polarity reversal results from action that takes place at the reflector: first, the P-wave polarization vector (direction of particle motion) is projected on to the reflecting plane, and then the motion along the reflector is projected on to the S-wave polarization vector. The projections involve, first, sine of the P-wave incidence angle at the reflector and, second, cosine of the S-wave reflection angle. (A third factor con-

tributes to the final recorded amplitude. This is the receiver directivity, cosine of the S-wave emergence angle, which projects particle motion on to the horizontal receiver component.) The product of these factors accounts for both the observed polarity reversal and an amplitude factor. To correct for this effect, the inverse of the projection process should be applied before or (preferably) during imaging. In premigration processing the correction is approximated by a radial/transverse projection of the two horizontal components of the recorded data, retaining the radial component. In 2D, this correction reduces to a polarity reversal of the data at negative offsets. Although this correction is often adequate (and is used in our examples), it ignores polarity reversals that occur at nonzero offsets and can be improved in PS beam migration. The P- and S-wave polarization vectors, or good approximations, are available during Gaussian beam ray tracing and imaging. These can be used first to compute incidence and reflection angles at each image location, as well as reflector dip and azimuth, and next to apply the amplitude correction, including the sign change as incidence angle passes through zero. The correction, which reciprocates the product of sine and cosine, becomes singular at zero incidence angle, and so it must be tapered to zero near normal incidence. The error of applying the taper is negligible because the P–S reflection coefficient is equal to zero at normal incidence at the reflector and is very small near normal incidence, contributing little energy to the migrated image.

S-WAVE MODELING AND MIGRATION FOR WEAK AND STRONG ANISOTROPY

Ray tracing in inhomogeneous anisotropic media is the essential building block for seismic modeling and imaging with Gaussian beams. Traditionally, ray tracing in anisotropic media has been formulated in terms of the 21 elastic parameters (Červený 2001), making it applicable to the most general lower anisotropy symmetry. However, the elastic-parameter-based formulation of the eikonal equation is not compatible with the bulk of seismic processing, which usually uses Thomsen's (1986) parameters to describe both P- and S-wave anisotropy. In addition, the full elastic version of the eikonal equation is cumbersome for ray tracing, requiring evaluation of complicated right-hand-side functions and solution of an eigenvalue problem at each ray step.

Zhu *et al.* (2007) overcome these difficulties for P-wave ray tracing by basing the eikonal equation on phase velocity, for which there exist simple analytical expressions involving Thomsen parameters for transverse isotropic (TI) and orthorhombic media. We follow this approach to obtain the governing ray equations for SV-waves in inhomogeneous TI media. Kinematic ray tracing is formulated as a system of ordinary differential equations, which are the first derivatives of the Hamiltonian (Pšenčík and Farra 2005)

$$H(\mathbf{x},\mathbf{p}) = \|\mathbf{p}\|^2 v^2(\mathbf{x},\mathbf{n}) - 1 = G(\mathbf{x},\mathbf{p}) - 1 = 0, \tag{5}$$

with respect to position $\mathbf{x}$ and slowness vector $\mathbf{p}$. Function $G(\mathbf{x},\mathbf{p}) = \|\mathbf{p}\|^2 v(\mathbf{x},\mathbf{n})^2$ is the phase velocity eikonal that, in a heterogeneous anisotropic medium, depends on medium properties at $\mathbf{x}$ and on the wave unit vector $\mathbf{n} = \mathbf{p}\|\mathbf{p}\|^{-1}$. Dynamic ray tracing equations are obtained by second derivatives of equation (5) with respect to $\mathbf{x}$ and $\mathbf{p}$ (equations 10 and 12 of Zhu (2010)), producing complex-valued Gaussian beam travel times and amplitudes. We use the same initial conditions for these as Hill (2001, Appendix A).

In a TI medium, the phase velocity varies with angle θ between slowness vector and symmetry axis $\mathbf{c}$ (Thomsen 1986). The phase velocity function is the same in all planes containing the symmetry axis, whereas in the orthogonal plane, it is isotropic. Moreover, symmetry axis $\mathbf{c}$ can be arbitrarily oriented according to different geological properties of the subsurface. In a TI medium, P- and SV-waves are coupled and so are their phase velocity and eikonal functions. The latter are given by

$$\begin{aligned} 2G_{\pm}(\mathbf{x},\mathbf{p}) = V_{P0}^2\{&2(1-f)\mathbf{p}^T\mathbf{p} + f\mathbf{p}^T\mathbf{p} + 2\varepsilon(\mathbf{p}^T\mathbf{p} - (\mathbf{p}^T\mathbf{c})^2) \\ &\pm\sqrt{(f\mathbf{p}^T\mathbf{p} + 2\varepsilon[\mathbf{p}^T\mathbf{p} - (\mathbf{p}^T\mathbf{c})^2])^2 - 8f(\varepsilon-\delta)(\mathbf{p}^T\mathbf{c})^2(\mathbf{p}^T\mathbf{p} - (\mathbf{p}^T\mathbf{c})^2)}\}, \end{aligned} \tag{6}$$

where ε and δ are Thomsen parameters, $f = 1 - \frac{V_{S0}^2}{V_{P0}^2}$ depends on P- and S- wave velocities along the symmetry axis $\mathbf{c}$, and $\cos^2\theta = \frac{(\mathbf{p}^T\mathbf{c})^2}{\mathbf{p}^T\mathbf{p}}$, given angle θ between phase vector $\mathbf{n}$ and the direction of the symmetry axis. The sign of the square root specifies the P- (+) or the S- (-) wave phase velocities, respectively (Tsvankin 2006).

In the limit of weak anisotropy, equation (6) decouples into two separate expressions for the P- and SV-wave eikonals:

$$\begin{aligned} G_P(\mathbf{x},\mathbf{p}) = V_{P0}^2\Big(&\mathbf{p}^T\mathbf{p} + 2\delta\left(\mathbf{p}^T\mathbf{c}\right)^2\left(\mathbf{p}^T\mathbf{p} - \left(\mathbf{p}^T\mathbf{c}\right)^2\right) \\ &+ 2\varepsilon\left(\mathbf{p}^T\mathbf{p} - \left(\mathbf{p}^T\mathbf{c}\right)^2\right)^2\Big), \end{aligned} \tag{7a}$$

$$G_{SV}(\mathbf{x},\mathbf{p}) = V_{S0}^2\left(\mathbf{p}^T\mathbf{p} + 2\sigma\left(\mathbf{p}^T\mathbf{c}\right)^2\left(\mathbf{p}^T\mathbf{p} - \left(\mathbf{p}^T\mathbf{c}\right)^2\right)\right), \tag{7b}$$

where $\sigma = \frac{V_{P0}^2}{V_{S0}^2}(\varepsilon - \delta)$. We observe that equation (7b) has the same form as equation (7a) (Tsvankin 2006) if we apply the substitution $V_{P0} \leftarrow V_{S0}$, $\delta \leftarrow \sigma$ and set $\varepsilon = 0$. This approach provides a computational advantage, allowing the use of any

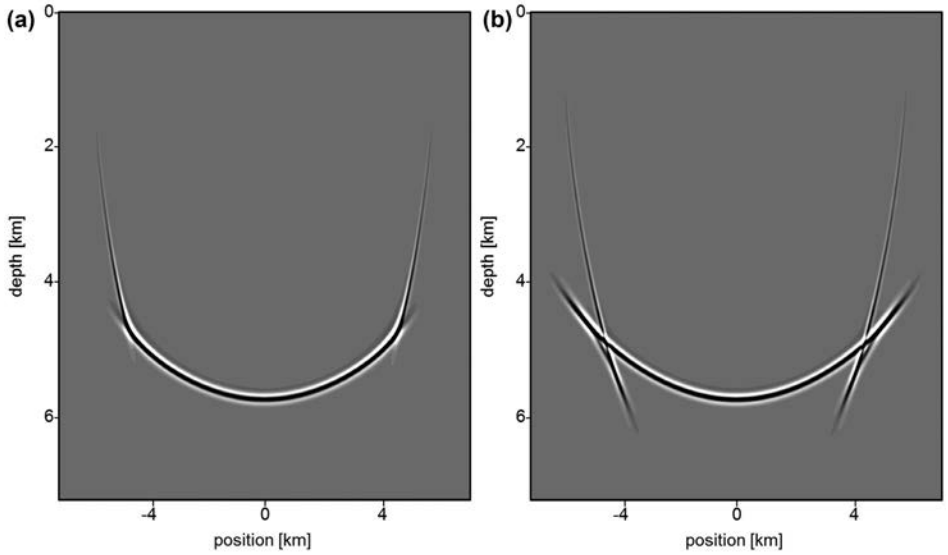

Figure 1 PS GBM zero-offset impulse response comparison in a homogeneous VTI model: $V_{P0} = 4336$ ms^{-1}, $V_{S0} = 1800$ ms^{-1}, $\delta = 0.01$, and $\varepsilon = 0.247$. An 8-Hz Ricker wavelet at time 4500 ms is the input for the migration. (a) Obtained using the weak anisotropy P- and S-wave equations (7a and b). (b) Obtained using the exact formulation for the P- and S-wave equations (6). The weak anisotropy approximation fails to accurately produce the wave surface. "Position" refers to the signed distance from the midpoint location.

existing P-wave modeling code to compute S-wave kinematics in weak anisotropy. Two different velocity models can then be used to compute PS travel times in beam migration: a P-wave $(V_{P0},\ \delta, \varepsilon, c_x, c_y)$ model for source-side P-wave rays and an S-wave $(V_{S0},\ \sigma, 0, c_x, c_y)$ model for receiver-side S-wave rays, where c_x and c_y are inline and crossline symmetry axis cosines. This approximation, however, breaks down where TI anisotropy is strong and can compromise the quality of the final image, especially in the presence of S-wave triplications (Fig. 1) and steep structures with lateral velocity variation (shown later in Figs. 7 and 8). In these situations, the exact or strong anisotropy S-wave ray tracing formulation based on equation (6) is preferred, and we use it for the PS imaging examples, which follow unless otherwise specified.

For modeling and migration using strong TTI, both standard Kirchhoff migration and RTM have significant problems with P- and/or S-waves. For Kirchhoff migration, the presence of anisotropy affects S-wave travel times more than it affects P-wave travel times. Unlike P-wavefronts, triplications in S-wavefronts are physically plausible in homogeneous media or in the presence of moderate lateral velocity variations. Interpolating triplicated S-wave travel times from a cone of ray paths on to a single-valued table on the migration grid can cause greater travel-time discontinuities than for P-wave migration, leading to a high level of PS Kirchhoff migration noise. For RTM, many industry applications propagate P-wavefields using a finite-difference solution of an "acoustic" wave equation with V_{S0} set to zero along the symmetry axis (e.g., Alkhalifah 2000; Fowler *et al.* 2010; Zhang, Zhang, and Zhang 2011). These wavefield extrapolators cannot decouple P-wavefronts from diamond-shaped S-wave artefacts (Grechka, Zhang, and Rector 2004), which have nonzero phase and group velocity in acoustic TI media. Stable propagation of an acoustic TI P-wave requires $\varepsilon > \delta$ in order to keep the medium stiffness matrix positive definite, as required by the medium energy constraint. Moreover, it is necessary to suppress unwanted S-wave arrivals before applying the imaging condition (Zhang *et al.* 2009; Khalil *et al.* 2013) to reduce crosstalk noise in the final image. For S-wave propagation in RTM, the acoustic P-wave formulation can be adapted to weak anisotropy as previously described, but there is no such adaptation for strong anisotropy. In addition, if P-wave velocity V_{P0} is set to zero along the symmetry axis, numerical stability requires $\delta > \varepsilon$ (the opposite of the TI P-wave stability condition). It can be shown that a nonzero V_{P0} can improve the stability of the S-wave "acoustic" wave equation, but this results in a P-wave-type noise that needs to be suppressed before the imaging condition is applied.

Until the problems with anisotropic S-wave wave propagation in RTM are resolved, the S-wave modeling formulation based on Gaussian beam ray tracing provides a more suitable framework than either Kirchhoff or finite-difference RTM methods for producing reliable PS subsurface images.

MULTIPATHING ILLUSTRATED: A CANONICAL ANALYTICAL EXAMPLE

Hill (2001) illustrates the ability of isotropic COV P-wave GBM to handle multipathing in a canonical situation. Here we similarly illustrate the ability of common-receiver PS and SS GBM to handle more severe multipathing due to SV-wave anisotropy.

Alternative versions of common-receiver GBM produce different accuracy values in the final image when the S-wavefield from a receiver location becomes arbitrarily complex. The accuracy and efficiency of common-receiver GBM implementations (plural) rely on the computation of integrals in equations (3) and (4). Direct evaluation of these would require accumulating on to the migration output grid a weighted version of the slant-stacked data $D_{\mathrm{r}}(\mathbf{p}^s;\mathbf{r},\omega)$ for each admissible ray pair $\mathbf{p}^s$, $\mathbf{p}^r$. Formally, this means evaluating a quadruple integral in the shot and receiver ray parameters at each beam centre location $\mathbf{L}$:

$$I_{\mathrm{r}}(\mathbf{x}) \approx -\frac{2C_0}{\pi}\sum_{\mathrm{L}}\int i\omega\, d\omega \times\int\int \frac{dp_x^s dp_y^s}{p_z^R}\int\int dp_x^r dp_y^r\, A^*_{PS}(\mathbf{x})\exp\left[i\varphi^*_{PS}(\mathbf{x})\right]\, D_{\mathrm{r}}(\mathbf{p}^{\mathbf{s}};\mathbf{L},\omega). \tag{8}$$

For clarity, we simplified the notation for the product $A_{PS}(\mathbf{x}) = A_{PS}(\mathbf{x},\mathbf{p}^s,\mathbf{p}^r;\mathbf{L})$ and sum $\varphi_{PS}(\mathbf{x}) = -\omega T_{PS}(\mathbf{x},\mathbf{p}^s,\mathbf{p}^r;\mathbf{L})$ of the P-wave source-side and the S-wave receiver-side Gaussian beam complex amplitudes and phases defined below equation (2). These quantities are computed by ray tracing using strong TI eikonal equations (6).

Neglecting the cost of ray tracing, direct evaluation of equation (8) involves $O(N_{\mathrm{ps}}\times N_{\mathrm{pr}})$ add/multiply operations, which is affordable for 2D or narrow-azimuth 3D migration. However, for 3D wide-azimuth seafloor surveys, the operation count increases super-linearly, quickly becoming unacceptably high.

We can reduce the computational load of equation (8) to $O(N_{\mathrm{ps}}+N_{\mathrm{pr}})$ operations in either of two ways. In the first, we replace the superposition of contributions from all values of $\mathbf{p}^r$ by an asymptotic approximation obtained from the steepest descent evaluation of the $\mathbf{p}^r$-integral around an assumed saddle point, located at critical value $\mathbf{p}^{r0}$. For common-receiver GBM, this is a natural analogue to Hill's (2001) approach to increase the efficiency of COV migration. For 3D GBM, it is possible to evaluate the $\mathbf{p}^r$-integral asymptotically by iterating a steepest descent approximation in variables p_x^r and p_y^r (Bleistein 2012), which simplifies equation (8) to

$$I_{\mathrm{r}}(\mathbf{x}) \approx -\frac{2C_0}{\pi}\sum_{\mathrm{L}}\int d\omega \times\int\int \frac{dp_x^s dp_y^s}{p_z^R}\, W^*_{PS}(\mathbf{x};\mathbf{p}^{r0})\exp[i\varphi^*_{PS}(\mathbf{x};\mathbf{p}^{r0})]\, D_{\mathrm{r}}(\mathbf{p}^s;\mathbf{L},\omega), \tag{9}$$

where $\mathbf{p}^{r0}$ is the critical value of the ray-parameter vector, at which surfaces of the real and imaginary parts of the total source–receiver phase $\varphi_{PS}(\mathbf{x};\mathbf{p}^{r0}) = -\omega T_{PS}(\mathbf{x},\mathbf{p}^{r0})$, considered as real-valued functions of the complex variable $\mathbf{p}^r$, form saddle shapes. Exactly at the saddle point, the real part of φ_{PS} has a local maximum whereas the imaginary part has a local minimum. The term $W_{PS}(\mathbf{x};\mathbf{p}^{r0})$ is a complex weighting factor. Equation (9) is a sub-optimal imaging formula in the presence of significant multipathing, as we show next using an analytic example. After that, we present an improved formula.

Figure 2a depicts a situation where strong anisotropy in a homogeneous half-space gives rise to inflection points in the S-wave phase velocity, causing triplication of travel times at propagation angles of approximately 45°. (Thus, the multipathing in this example is due to anisotropy not ray bending.) For this 2D example, we compare the evaluation of full expression (8) with its approximation (9). The source wavefield is represented by P-wave Gaussian beams radiating from location $\mathbf{x}_S = (-1000\,\mathrm{m},\ 0\,\mathrm{m})$, and the receiver field is represented by S-wave beams radiating from a receiver at beam centre location $\mathbf{L} = (+1000\,\mathrm{m},\ 0\,\mathrm{m})$. Figure 2a shows the P-wave (red) source-side p_x^s and S-wave (green) receiver-side p_x^r ray paths, with identical spacings in both p_x^s and p_x^r. The dashed lines are P- and S-wavefronts at 1.0 second and 4.336 seconds, respectively. Cusps in the S-wavefronts are from multiple arrivals at image locations. A maximum ray angle of 90° refers to a maximum possible S-wave ray parameter value of $p_x^s = 1/1800$ s/m. Figure 3a maps the magnitude of the integrand in equation (8) as a function of source-side and receiver-side ray parameters at $\mathbf{x} = (-4500\mathrm{m},\ 6000\,\mathrm{m})$, i.e., the location of the black box in Fig. 2a. The presence of three large peaks in Fig. 3a confirms that image point $\mathbf{x}$ is affected by three receiver-side arrivals caused by the S-wave cusps. Evaluating equation (8) directly, without asymptotic approximation, includes all the integrand contributions appearing in Fig. 3a, resulting in the GBM impulse response in Fig. 4a. For each value of source ray parameter p_x^s, all values of p_x^r contribute to the image at each image location. On the other hand, the steepest descent approximation in equation (9) allows a single (dominant) p_x^r-contribution to the image for each

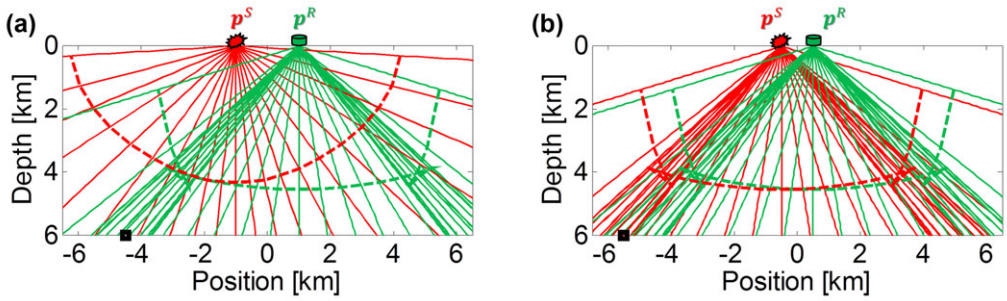

Figure 2 Source- and receiver-side rays. (a) P-wave (red) and S-wave (green) rays in a homogeneous canonical VTI model, with $V_{P0} = 4336\ \mathrm{ms}^{-1}$, $V_{S0} = 1800\ \mathrm{ms}^{-1}$, $\delta = 0.0$, and $\varepsilon = 0.247$. A maximum ray angle of 90° is related to a maximum possible value for the ray parameter of $p_x = \frac{1}{V_{S0}} sm^{-1}$. Source–receiver offset is 2000 m. The dashed lines are P- and S-wavefronts at 1.0 second and 4.336 seconds, respectively. (b) The P-wave shot point has been replaced by an S-wave source in order to illustrate the limitations of approximation (9). Source–receiver offset has been reduced to 1000 m.

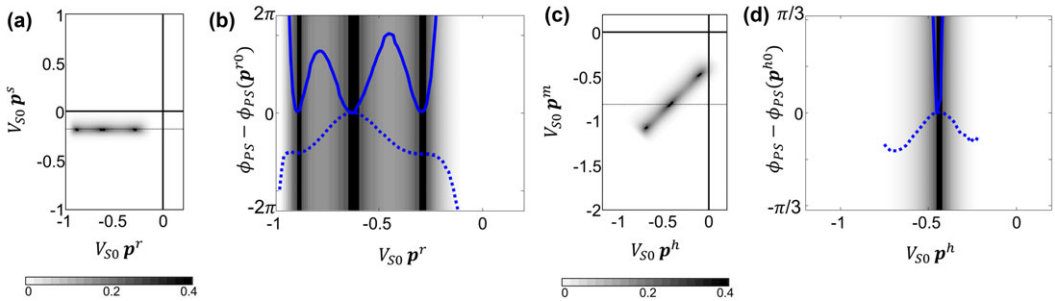

Figure 3 PS canonical example from Fig. 2a: numerical analysis for migration integral (8) evaluated at image location $\mathbf{x} =$ (-4500 m, 6000 m), with velocity and anisotropy parameters identical to those in Fig. 2a. (a) Magnitude of the integrand in equation (8) computed in the shot-receiver ray parameter domain. (b) Real (dashed line) and imaginary (solid line) parts of complex phase $\phi_{PS}(\mathbf{x})$ along constant $V_{S0}\mathbf{p}^s = -0.194$ path through the peak amplitudes in (a). (c) Magnitude of the integrand in equation (8) computed in the midpoint-offset ray parameter domain. (d) Real (dashed line) and imaginary (solid line) parts of complex phase $\phi_{PS}(\mathbf{x})$ along constant $V_{S0}\mathbf{p}^m = -0.820$ path through the peak amplitudes in (c). The time axis in (b) and (c) is scaled by a reference frequency $\omega_r = 2\pi\ 8\ hz$. The greyscale density in (b) and (c) corresponds to the magnitude of the integrand in equation (8).

p_x^s at each image location, namely, the term whose complex phase $\varphi_{PS}(\mathbf{x}; \mathbf{p}^{r0})$ has the minimum imaginary part over all values of p_x^r. If there were a single isolated peak in the integrand amplitude along p_x^r, then steepest descent approximation (9) would be a good one. That is not the case here, and the resulting impulse response, shown in Fig. 4b, shows the effects of the inadequate treatment of multipathing using equation (9).

To illustrate further, Fig. 3a refers to image location $\mathbf{x} = (-4500\,\mathrm{m},\ 6000\,\mathrm{m})$. For $V_{S0}\,p_x^s = -0.194$, the summation path over variable $V_{S0}\,p_x^{r0}$ (dotted line in Fig. 3a) intersects three candidate stationary points. The minimum value of the imaginary part of phase $\varphi_{PS}(\mathbf{x}; p_x^{r0})$ occurs at $V_{S0}\,p_x^{r0} = -0.626$ (solid blue line in Fig. 3b), at which point the value of complex travel time is $T_{PS}(\mathbf{x}; p_x^r) = 5.061 + i0.016$ (solid and dashed blue lines in Fig. 3b). This is the only value of travel time used in approximation (9), which neglects valid contributions from slightly smaller peaks occurring at $V_{S0}\,p_x^r = -0.896$ and $V_{S0}\,p_x^r = -0.302$, caused by the correlation between late-arriving beams from the S-wave side. Values of $V_{S0}\,p_x^s$ close to -.0194 might accumulate any one of the peak contributions to the image at $\mathbf{x}$, with similar confusion suffered at neighboring image locations, creating harsh discontinuities and jitter in the GBM impulse response (Fig. 4b). In general, the receiver-side steepest descent approximation in equation (9) accumulates only one (in this case, the most energetic) contribution from the receiver side (Nowack, Sen, and Stoffa 2003) at any image location, affecting the GBM impulse response with the same sort of branch jumping that we often see with single-arrival Kirchhoff migration.

To improve on this version of common-receiver GBM, Gray (2005) suggested using the same computational structure that Hill (2001) uses for COV migration. Formally we apply a midpoint-offset ray-parameter rotation $\mathbf{p}^m = \mathbf{p}^s + \mathbf{p}^r$ and $\mathbf{p}^h = \mathbf{p}^s - \mathbf{p}^r$ to equation (8) to obtain an integration in the midpoint-offset ray-parameter domain, which we

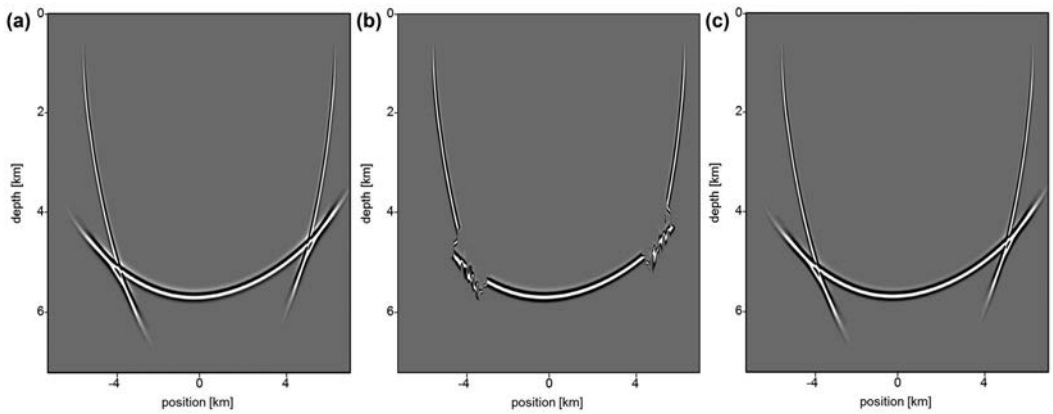

Figure 4 PS GBM impulse response comparison in homogeneous VTI model: $V_{P0} = 4336\ \mathrm{ms}^{-1}$, $V_{S0} = 1800\ \mathrm{ms}^{-1}$, $\delta = 0.01$, and $\varepsilon = 0.247$. An 8-Hz Ricker wavelet at time 4500 ms is the input for the migration. Source and beam centre location are 2000 m apart. (a) The full numerical evaluation of integral (8) maps all the PS-wavefront branches related to the S-wave cusps. (b) The receiver-side steepest descent approximation (9) misses the later-arriving S-wave cusps, resulting in harsh branch jumping. (c) The offset-domain steepest descent approximation (10) recovers the cusps missed by equation (9).

approximate by performing a steepest descent integration over offset ray parameters, yielding

$$I_{\mathrm{r}}(\mathbf{x}) \approx -\frac{C_0}{4\pi}\sum_{\mathrm{L}}\int d\omega \times\int\int \frac{dp_x^m dp_y^m}{p_z^r}\, W_{PS}^{*}(\mathbf{x};\mathbf{p}^{b0})\exp\left[i\varphi_{PS}^{*}(\mathbf{x};\mathbf{p}^{b0})\right]\, D_{\mathrm{r}}(\mathbf{p}^{s};\mathbf{L},\omega). \quad (10)$$

In most cases, equation (10) retains more multipath arrivals than equation (9). For our 2D canonical example, Fig. 3c shows a remapping of the magnitude of the integrand in equation (7) as a function of midpoint-offset ray parameters at the same image location $\mathbf{x} = -(4500\,\mathrm{m},\ 6000\,\mathrm{m})$ as before. The variable change has resulted in a 45° counterclockwise rotation of the three large peaks from their original aligned locations in the shot-receiver ray parameter space (Fig. 3a) to locations with distinct values of p_x^m (Fig. 3c). For each midpoint ray parameter p_x^m, steepest descent integral (10) retains the dominant contribution from the offset ray parameters; these contributions appear as isolated saddle points, making the approximation accurate and the migrated impulse response (Fig. 4c) reliable. For example, the previously chosen shot-receiver minimum imaginary travel time $T_{PS}(\mathbf{x};p_x^{r0}) = 5.061 + i0.016$ peak at $V_{S0}\,p_x^{so} = -0.194$ and $V_{S0}\,p_x^{r0} = -0.626$ (Fig. 3b) is mapped to midpoint ray parameter location $V_{S0}\,p_x^{m0} = -0.820$ for which complex phase $\varphi_{PS}(\mathbf{x};p_x^{b0})$ has an isolated saddle point at $V_{S0}\,p_x^{b0} = -0.435$ (Fig. 3d).

Despite its improved accuracy, approximation (10) is still prone to error when both source- and receiver-side beams are multivalued. To illustrate this, we complicate the canonical example by replacing the source-side P-wave beams with an S-wave shot point (Fig. 2b). Then we compare SS-wave GBM integrand (Fig. 5a and b) and impulse responses (Fig. 6a and b) from integral (8) and approximation (10). Figure 5a shows the magnitude of the SS-wave integrand in equation (8) as a function of the midpoint-offset ray parameters at image location $\mathbf{x} = -(5500\,\mathrm{m},\ 6000\,\mathrm{m})$, i.e., the location of the black box in Fig. 2b. As expected, three arrivals from both shot and receiver beams combine to form a surface with nine peaks. Six of these peaks are related to isolated saddle points, which approximation (10) can correctly include in the final image. However, the p_x^b -integration path for $V_{S0}\,p_x^{m0} = -1.120$ cuts the integrand surface close to three candidate saddle points (Fig. 5a); all will be used in equation (8), but only one will be used in equation (10). Figure 5b shows that the candidate at $V_{S0}\,p_x^b = +0.529$ has the largest value for the integrand and the smallest value of imaginary time. For slightly different values of $V_{S0}\,p_x^{m0}$, one of the other two candidates will be chosen, leading to jumps in real travel time and causing the mild branch jumping barely evident in the GBM impulse response in Fig. 6b.

To summarize, the integration path along the midpoint ray parameter $\mathbf{p}^m$ usually captures most multiple wavefield arrivals that are due to multipathing from either source side or receiver side. Therefore, GBM using approximation (10)

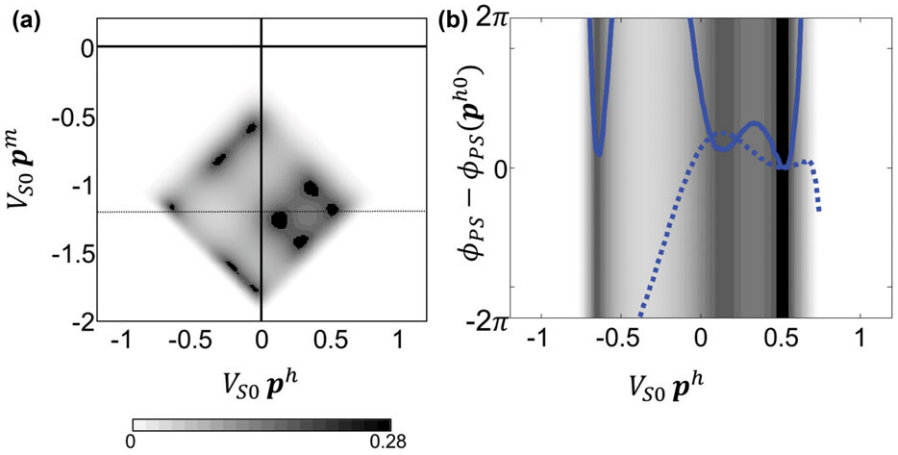

Figure 5 SS-wave canonical example from Fig. 2b: numerical analysis for the migration integral (8), evaluated at image location $\mathbf{x} =$ (-5500 m, 6000 m), with velocity and anisotropy parameters identical to those in Fig. 2b. (a) Magnitude of the integrand in equation (8) computed in the midpoint-offset ray parameter domain. (b) Real (dashed line) and imaginary (solid line) parts of complex phase ϕ_{PS} (**x**) along constant $V_{S0}\mathbf{p}^m = -1.120$ path through the peak amplitudes in (a). The time axis is scaled by a reference frequency $\omega_r = 2\pi\ 8hz$. The greyscale density in (b) corresponds to the magnitude of the integrand in equation (8).

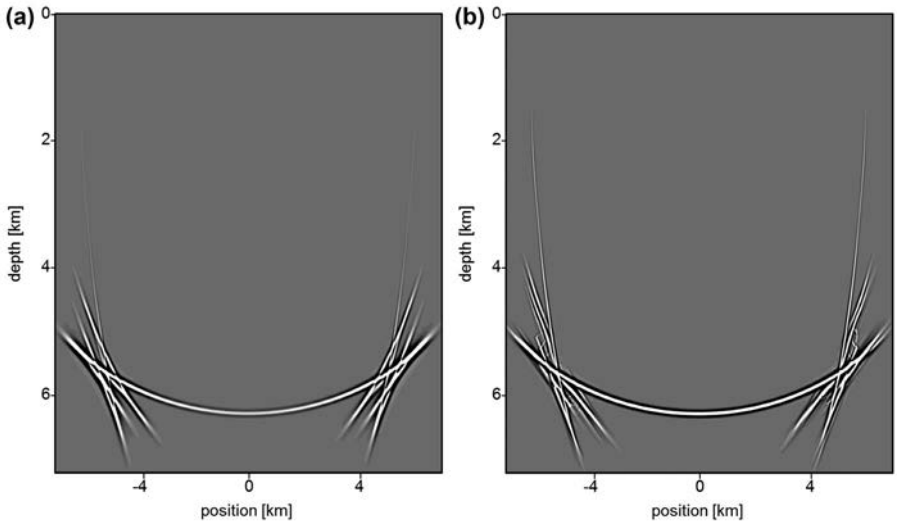

Figure 6 SS-wave GBM pre-stack impulse response comparison in homogeneous VTI model: $V_{P0} = 4336\ ms^{-1}$, $V_{S0} = 1800\ ms^{-1}$, $\delta = 0.01$, and $\varepsilon = 0.247$. An 8-Hz Ricker wavelet at time 4500 ms is the input for the migration. Source and beam centre location are 1000 m apart. (a) The full numerical evaluation of integral (8) maps all nine SS-wavefront branches caused by the correlation of the three S-wave arrivals from each of the shot and the receiver locations. (b) The offset-domain steepest descent approximation (10) misses some combination of source- and receiver-side arrivals, resulting in a mild branch jumping.

improves accuracy over equation (9) by reducing branch jumping, with the same algorithm operation count. An extra cost is required to keep track of the critical receiver ray parameter $\mathbf{p}^{r0}$ for each stationary midpoint-offset $\mathbf{p}^m$, $\mathbf{p}^{h0}$ pair. In the following OBN synthetic and field dataset examples, our GBM implementation uses approximation (10).

AN OCEAN BOTTOM ACQUISITION SYNTHETIC EXAMPLE

This section describes a PS "controlled-beam migration" (CBM) result from an OBN 2D TTI elastic synthetic dataset. CBM is a specialized version of GBM that enhances the signal-to-noise ratio of imaged geological structures by keeping

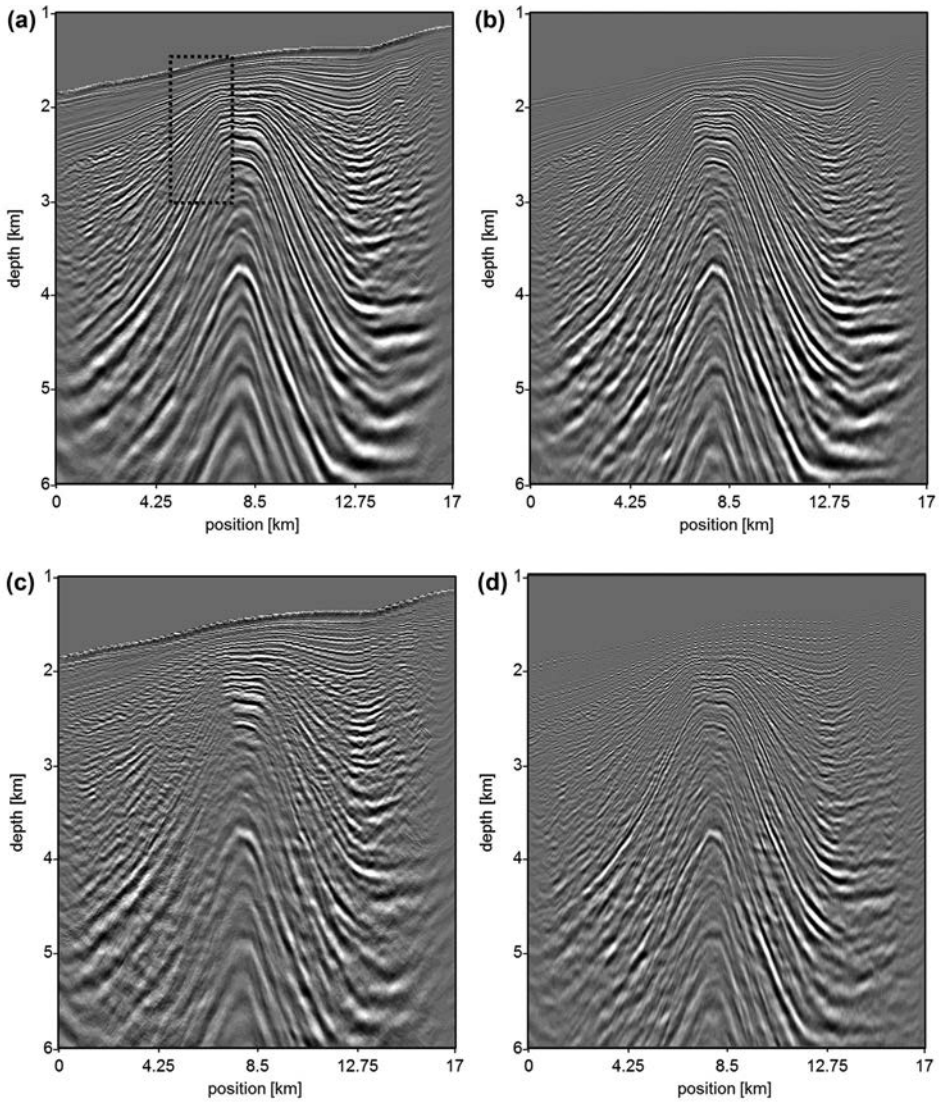

Figure 7 OBN 2D synthetic stacked sections after PS migration, with receiver spacing of 100 m in (a and b) and 300 m in (c and d). (a and c) Common-offset migration. (b and d) Common-receiver migration. At 300-m receiver spacing, common-receiver migration recovers the steeply dipping deep structures better than common-offset migration.

migration operator noise low (Vinje, Roberts, and Taylor 2008). Comparison between common-offset and common-receiver imaging illustrates the advantages of the latter when receiver spacing becomes coarse (~300 m–400 m).

The dataset consists of 170 OBN records, with nodes at depths between 1375 m and 1837 m, and 1280 shots at a depth of 12.5 m. Shot and receiver sampling are 12.5 m and 100 m, respectively. The sea bottom is gently dipping with an average dip of 1.6°, but significant subsurface structure is present (Fig. 7). The velocity model follows a compaction trend: $V_{P0}/V_{S0} = 5$ at the seafloor and $V_{P0}/V_{S0} = 2$ in the deeper section. The TI anisotropy is partly aligned with geologic structure and partly compaction driven. Values of anellipticity $\eta \approx \varepsilon - \delta$ range from 10% to 25%.

We applied common-offset CBM to horizontal component records from this dataset. We also applied data pre-processing and CBM to common-receiver gathers to compare the effects of different receiver spacings on migration in the two domains. A radial/downgoing (Amundsen 2001) deconvolution was applied to attenuate P-wave surface-related multiples, but residual multiple energy and other P-wave energy surviving the pre-processing were migrated, generating cross-talk noise in the depth image.

Our imaging test includes two scenarios: (i) OBC-like acquisition, with receivers 100 m apart from each other; and (ii) OBN-like acquisition, in which we decimate receiver spacing to 300 m. In each scenario, we compare and discuss the imaging performance and reliability of common-offset and common-receiver PS CBMs. All results are obtained using S-wave beam modeling based on the eikonal equation (6) (strong anisotropy) unless otherwise specified.

Figure 7a and b illustrates the OBC scenario; receiver spacing is 100 m. Figure 7a shows the stacked section after common-offset CBM. The 100-m receiver spacing leads to a natural 2D offset tile size of 200 m. Positive and negative offset planes (maximum offset is ±8000 m) were migrated separately. The final stacked image results from the sum of positive and negative stacks after approximate zero-offset polarity reversal. In order to make all offsets equal for traces in a given tile, we applied a kinematic offset centring by PS differential NMO correction before slant-stacking at each beam centre location. This has the effect of reducing kinematic jitter within each offset tile; the result is a good-quality image, even at depths just below the seafloor where illumination is most irregular. Figure 7b was produced by common-receiver CBM of all the 170 gathers in the dataset. The two images are nearly equivalent, both showing good continuity and resolution with low noise for shallow reflectors and the sequence of steep-dipping anticline flanks. The common-offset migrated image shows slightly less migration aliasing noise than the common-receiver migrated image because the natural spacing within offset tiles (12.5 m) is less than the 100-m spacing of the receivers. Other than that difference, we hypothesize that for a normal cable receiver spacing (~100 m), either common-offset or common-receiver migration can provide reliable PS images. This is because the OBC scenario approaches the limiting case of having the same sampling interval in midpoint and receiver domains, in which limit both images would be identical. Therefore, standard OBC acquisition does not require common-receiver PS migration for imaging; in fact, it appears to favor common-offset migration.

Figure 7c and d illustrates the OBN scenario; receiver spacing is 300 m. These images show stacked sections after common-offset CBM and common-receiver CBM, respectively. In Fig. 7c, the effect of increased receiver spacing on the PS differential NMO corrections is evident in the poor image of the steep flanks of the anticline. In Fig. 7d, the effect of increased receiver spacing on the imaging is less than for Fig. 7c, in agreement with our expectations for greater accuracy of migration than NMO-based interpolation in the presence of a complex structure.

Regardless of migration domain or receiver spacing, the use of weak anisotropy, particularly for S-waves, can affect the quality of focusing and positioning on the PS migrated image. Figure 8 shows (a and b) migrated stacks and (c and d) CIGs extracted from CBM-migrated volumes using (a and c) weak and (b and d) strong S-wave anisotropy. The offset-domain CIGs (ODCIGs) are sampled every 50 crosslines; they are extracted from the central part of the zoomed area marked by the black dotted square in Fig. 7a. The white arrows pinpoint some reflections for which weak and strong formulations of anisotropy have resulted in different kinematics and focusing of the two images. On the steep flanks, lateral displacements between the two images are on the order of 100 m. (A similar comparison of PP-migrated ODCIGs, using weak and strong anisotropy, produced negligible differences.) Although the weak anisotropy approximations have simpler expressions than strong anisotropy, producing slightly more efficient computations, the strong formulation is always preferable. Using the weak anisotropy approximation produces kinematic and focusing errors when the correct velocity fields are used; hence, we can expect it to bias a tomographic or full-waveform inversion whose goal is to estimate migration velocity.

FIELD DATASET EXAMPLE

Here we present and discuss imaging results from a PS depth migration and model building project on a deep-water 4C OBN field dataset. This prospect is located in the Central North Sea, approximately 150 km west of the Shetland Islands. The data were acquired in two phases using in total 1986 OBNs. Nodes were deployed on the seafloor (blue horizon in Figs. 9 and 10) on a regular grid with 300-m spacing both in crossline and inline. Guns were fired in a shot carpet configuration with source spacing of 30 m x 30 m.

The field geology is complex, and the primary target is an intra-basalt reservoir. The red and green horizons in Figs. 9 and 10 correspond to the top and base of the high-velocity volcanic region, where P-wave velocity rapidly increases from 2000 m/s to nearly 4000 m/s. Between these two horizons, a V_{P0}/V_{S0} value of 2 was deduced from well matching and event registration. Thin (~75-m thick) intra-volcanic sands challenge the resolving power of both P-wave and PS imaging. In principle, PS imaging resolution should exceed that of P-wave imaging because of the shorter S-wavelength, but in practice, the S-wave suffers from effects of higher absorption and birefringence, which degrade seismic resolution at the target level. A secondary deeper sub-basalt target reservoir

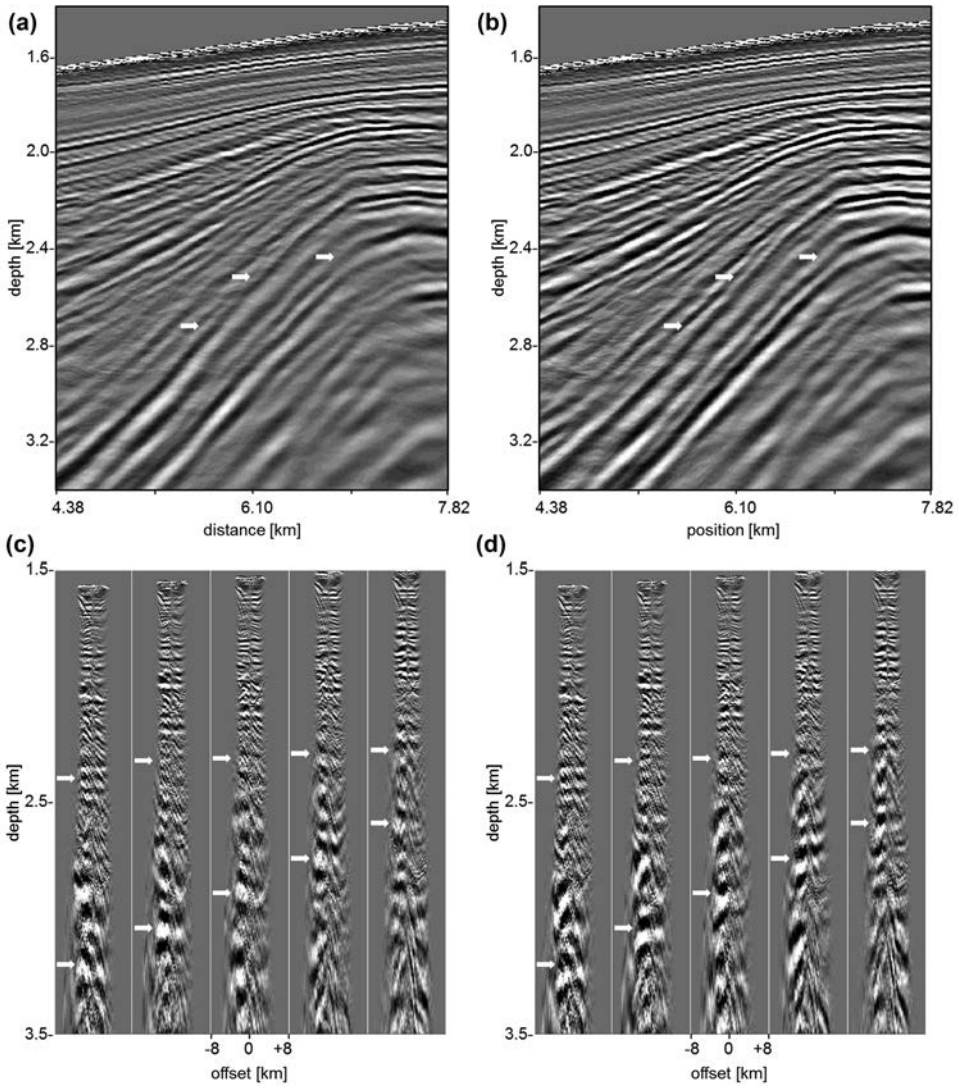

Figure 8 OBN 2D synthetic weak (a and c) and strong (b and d) PS anisotropy migration test. (a and b) Stack and (c and d) ODCIG after common-offset CBM migration. These images belong to the zoomed area marked by the black dotted square in Fig. 7a. ODCIGs are sampled every 50 crosslines The white arrows highlight some reflections for which the weak anisotropy S-wave modelling fails to position and focus accurately the steep flanks of the anticline.

benefits more from full azimuth illumination than the primary target does.

The shallow section presents the most difficult imaging and model building challenge. The sparse node acquisition compromises illumination near the seafloor for both upgoing P- and upgoing S-wavefields (Figs. 9 and 10). Three core samples estimated the S-velocity of the first consolidated layer to be roughly 128 m/s, resulting in $V_{P0}/V_{S0} \approx 12$. This high ratio forces S-waves to arrive at the receivers nearly vertically, further degrading lateral resolution of the PS data in the near surface. However, vertical resolution is exceptional. Mirror imaging of downgoing energy reflected from the sea surface can mitigate the near-surface imaging problems for P-waves (Dash *et al*. 2009) but no such downgoing S-waves can propagate in the water. (It is possible, in principle, to perform PS mirror imaging using S–P converted waves at the seafloor, but this requires extremely accurate and precise measurements of seafloor V_S.) For all these reasons, imaging OBN data with widely spaced nodes is extremely challenging.

After 3C vector rotation to radial and transverse components, we used the former for imaging. Moreover, 3D common receiver regularization, radial-down deconvolution, and

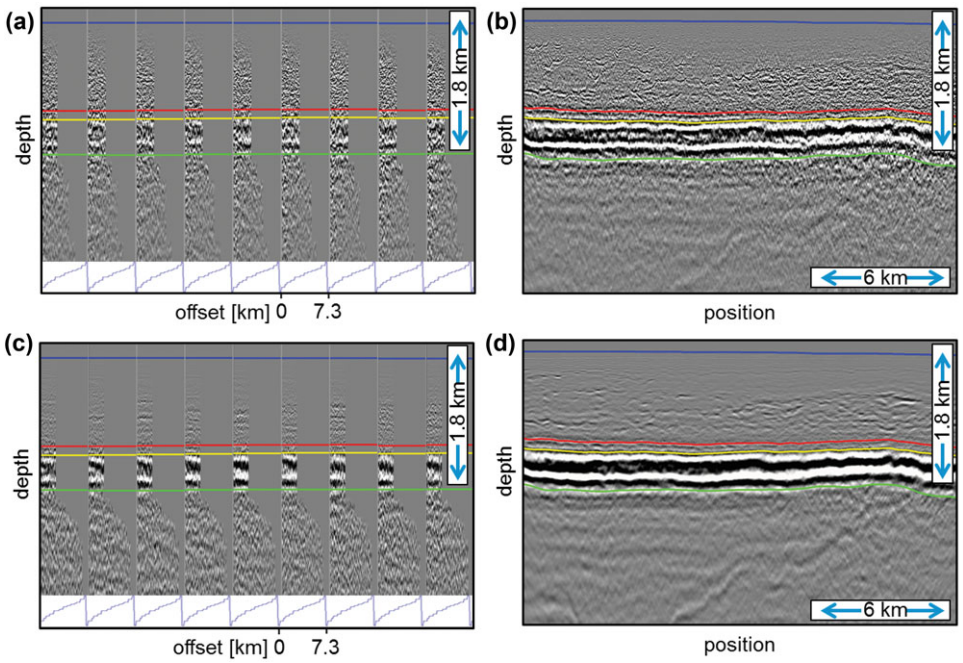

Figure 9 4C OBN 3D field dataset. PS Kirchhoff and CBM COV gathers (a and c) and stack image (b and d) for a crossline section. The data have been sorted in 10×10 COV tiles. CBM input COVs are single fold. The offset tile interval is 600 m x 600 m, and the maximum absolute offset is 7.29 km. The blue line depicts the seafloor horizon. Top, middle, and base of the sequence of volcanic rocks are highlighted by the red, yellow, and green horizons. The vertical scale in (d) is the same for all the plots, and the lateral scale in (d) is the same as in (b).

Q phase compensation were the major pre-processing steps for the radial component. Figure 9 shows a comparison between (a and c) PS Kirchhoff and CBM COV ODCIGs and (b and d) stacked images for a South–North crossline section. The data were sorted into 10 inline by 10 crossline COV volumes before migration in order to obtain ODCIGs for PS velocity model building. The coarse receiver spacing forces large OVTs (600 m x 600 m). As aforementioned, large OVTs have two separate negative effects on imaging and model building: (i) a large range of offset vectors within each tile of nominal x- and y-offsets; and (ii) a small number of traces (10 × 10 in this case) in each ODCIG. The first forces extensive regularization of the PS traces in order to build well-populated COV volumes for migration, which requires all offsets and azimuths within a COV volume to be the same. The second limits sensitivity of residual moveout analysis and tomographic velocity model updating. Testing with 5D regularization techniques (Trad 2009) showed that, for PS data, these techniques are least effective near the seafloor, where they are most needed. Depending on target depth, if receiver illumination cones overlap, PS data regularization can be effective (Casasanta and Grion 2012). For this example, however, we relied on a simpler regularization provided by differential PS NMO corrections. Even though these corrections are relatively crude for PS data, our testing showed them to be about as effective as corrections from more sophisticated regularization methods.

At primary target level, the COV CBM image (Fig. 9d) is more continuous than the Kirchhoff stack (Fig. 9b). Conversely, the Kirchhoff image preserves many of the near-surface high-frequency and steeply dipping structures while the CBM image suffers from lateral smearing induced by the PS regularization we used to precondition the COVs. Much of the Kirchhoff PS migration noise is due to interpolation of multivalued S-wave travel times from a narrow cone of rays on to a single-valued table on the migration grid, producing a large number of discontinuities. Deeper, the high-velocity basalt layer acts as a defocusing optical lens; thus, much of the seismic energy is reflected. The penetrating ray paths spread out rapidly within the basalt and are associated with complicated P-wave and S-wave wavefronts, some of them multi-branched. Below basalt, CBM outperforms standard Kirchhoff migration because of its intrinsic multi-arrival capability. This is most evident on the dipping reflectors beneath the basalt layer. This comparison illustrates how PS Kirchhoff and COV beam migration handle the trade-off

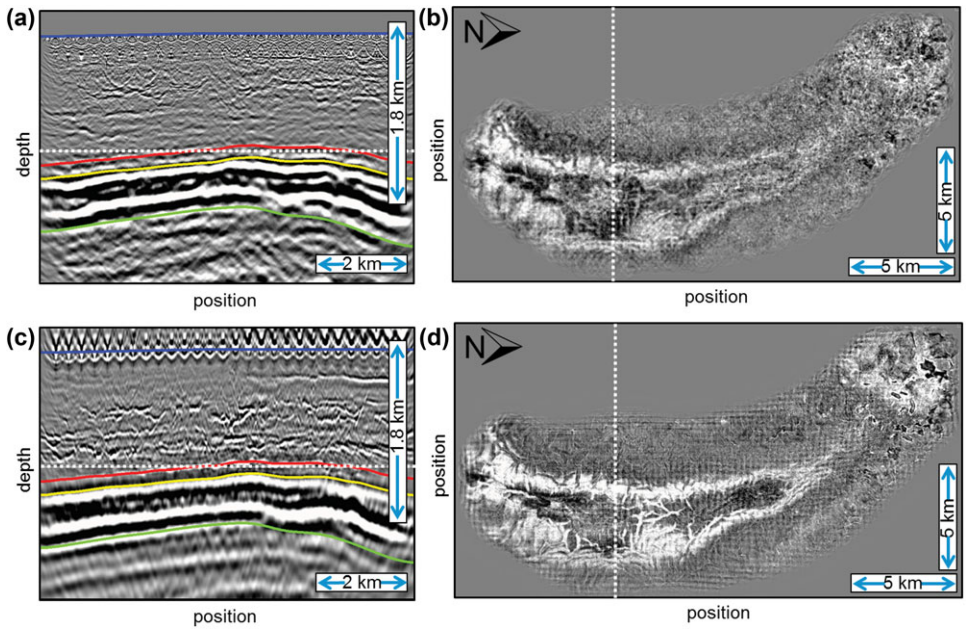

Figure 10 4C OBN 3D field dataset. (a and c) PS CBM and P-wave RTM inlines, respectively, at the location of the white dashed line in (b and d). (b and d) PS CBM and P-wave RTM shallow volcanic depth slices, respectively, at the depth of the white dashed line in (a and c). Both migrations used the final velocity model obtained after completion of all the model building units. P-wave RTM stack has been time-variant filtered in order to match the PS image spectrum. The color horizons are the same as in Fig. 9.

between image resolution and image noise for sparsely acquired seafloor data.

The uplift from CBM is more evident on the ODCIGs (Fig. 9a and c). The Kirchhoff gathers (Fig. 9a) are noisy at target level and residual moveout is hard to distinguish from noise at levels deeper than the target. Residual curvature tomographic autopickers will be prone to error when working on such noisy gathers. On the other hand, the RMO trend on the CBM gathers (Fig. 9c) is clearer and more easily picked, especially above target horizon, making a tomographic update using CBM picks more robust than an update based on the Kirchhoff gathers. The CBM gathers are cleaner than the Kirchhoff gathers for two reasons. First, the ability of beam migration to handle multipathing results in cleaner imaging overall, which is especially evident in low-fold migrated gathers. Second, as aforementioned, CBM is designed to enhance structural imaging while suppressing noise. From this comparison of migrated gathers, we expect that PS CBM will usually facilitate tomographic PS velocity model building.

In this project, the limited range and coarse sampling in ODCIGs residual curvature tomography provided limited leverage for updating the velocity model. Instead, we used a sequence of PS to P-wave image registrations to improve the S-wave velocity model at top, middle, and base (red, yellow, and green horizons in Fig. 10) of the sequence of volcanic rocks. Within each registration stage, we performed migration scans to estimate velocities and anisotropy parameters; these improved the focusing and positioning of the shallowest seismic structures. For these, we used common-receiver CBM, which provided clearer images than Kirchhoff migration.

As Fig. 10a shows, the shallow image from common-receiver CBM contains more detail than the COV CBM image (Fig. 9d), which suffers from smearing previously described. This is because common-receiver migration, which operates in the domain where data are best sampled, requires less data regularization than COV migration. As a result, common-receiver CBM preserves the original dip/azimuth richness of OBN data, resulting in greater wavenumber detail in the image than can be obtained with COV PS migration.

For calibration with P-wave imaging, Fig. 10 compares common receiver PS CBM and P-wave RTM images for, respectively, (a and c) an inline section in the southern part of the field (white dashed line in Fig. 10b and d) and (b and d) a depth slice near the top of the volcanic area (dashed line in Fig. 10a and c). Both migrations used the final velocity model obtained after completion of all the model building units. Considering the low-frequency content of the PS data, the P-wave RTM stack was depth-variant filtered in order to

match the PS image spectrum. Figure 10a and c show good co-positioning of C- and P-wave migrated horizons (red, yellow, and green lines) determined by the registration sequence, with greater continuity of shallow reflectors in the RTM image. The greater evidence of acquisition footprint on the P-wave image than on the PS-image is due to its lateral wavenumber content, which was not affected by the depth-varying filter.

Given the complex geology and uneven PS illumination below the nodes, horizon interpretation and consequent registration near the seafloor were prohibitively difficult. Accurate near-surface S-wave velocity estimation and PS imaging remain challenges for sparsely acquired data. While the narrow illumination provides high vertical resolution, it compromises our ability to extend knowledge of the model laterally. On the positive side, Fig. 10a and b show that the primary target thin sand layer (~1.8 km from the seafloor) is well resolved on the PS image. Moreover, detailed observation of depth slices such as those in Fig. 10b and d show that at medium depths, where uneven PS illumination starts healing, detailed features in the PS image (Fig. 10b) correlate well with corresponding features in the P-wave image (Fig. 10d). Given the large receiver spacing at the seafloor, PS lateral resolution is better than we originally thought achievable.

CONCLUSIONS

We have investigated the use of GBM for imaging marine PS data. We showed the modifications of P-wave GBM needed for PS imaging, particularly the importance of using equations (6) and (10) to account for the strong multipathing of S-waves. The ability of GBM to handle such multipathing gives it an advantage over conventional implementations of PS Kirchhoff migration, which tend to produce many discontinuities in its travel-time tables, resulting in noisy images. We also showed some advantages of GBM over RTM, both computational (the requirement of a fine grid for S-wave propagation and imaging) and theoretical (the inability of most RTM implementations to handle strong anisotropy in S-wave propagation).

We applied two GBM methods to the migration of PS data acquired on the seafloor, i.e., COV and common-receiver; each has advantages and disadvantages. COV migration requires data regularization before migration, which can be accomplished by residual PS NMO corrections for seafloor cable data with relatively fine receiver spacing. For seafloor node data with node spacing on the order of hundreds of meters, PS NMO corrections are inadequate, adversely affecting COV imaging at all depths. Common-receiver migration requires no data regularization before imaging and produces better images at all depths for node data than COV migration. On the other hand, COV migration produces ODCIGs as a natural by-product, and common-receiver migration does not, necessitating a velocity model building workflow that relies on migration scans and C- to P-wave image registration rather than analysing moveout on ODCIGs.

Our synthetic and field data examples illustrated the benefits of PS GBM and the relative merits of COV and common-receiver implementations. All examples showed that PS imaging of data acquired at the seafloor remains challenging, and the major problem is large receiver spacing, crossline for cable data, and both inline and crossline for node data. This separation causes an acquisition footprint that is visible on a migrated image. This will continue to be the case until receiver spacing is reduced to distances on the order of an S-wavelength at the seafloor.

ACKNOWLEDGEMENTS

The authors thank Sergio Grion for initiating this project. He strongly believed in the potential of Gaussian beam imaging for converted waves despite intrinsic limitations. They thank Chevron for providing the PS elastic synthetic dataset, and Chevron, Statoil, OMV, and Dong Energy for allowing the publication of the real data images. They also thank Jim Gaiser, Graham Roberts, Vetle Vinje, Ross Haacke, and Yu Zhang for stimulating discussions and critiques, and Pierpaolo Chiarandini, Naga Veera-Golla, Adel Khalil, and Simon Drummie for their support in processing the field dataset tests.

REFERENCES

Alkhalifah T. 2000. An acoustic wave equation for anisotropic media. *Geophysics* **65**, 1239–1250.

Amundsen L. 2001. Elimination of free-surface related multiples without need of the source wavelet. *Geophysics* **66**, 327–341.

Beasley C.J. and Mobley E. 1988. Amplitude and antialiasing treatment in (x-t) domain DMO. SEG, Expanded Abstracts, 1113–1116.

Bleistein N. 1984. *Mathematical Methods for Wave Phenomena*. Academic Press Inc.

Bleistein N. 2012. Saddle point contribution for an n-fold complex-valued integral http://www.cwp.mines.edu/Documents/cwpreports/cwp741.pdf

Burridge R., deHoop M.V., Miller D. and Spencer C. 1998. Multiparameter inversion in anisotropic media. *Geophysical Journal International*, 757–777.

Calvert A., Jenner E., Jefferson R., Bloor R., Adams N., Ramkhelawan R., *et al*. 2008. Wide azimuth imaging and azimuthal velocity analysis using offset vector tile prestack migration. *First Break* **26**, 103–107.

Cary P.W. 1999. Common-offset-vector gathers: an alternative to cross-spreads for wide-azimuth 3-D surveys. 69th SEG annual international meeting, Expanded Abstracts, SPRO-P1.6, 1496–1499.

Casasanta L. and Grion S. 2012. Converted-wave controlled-beam migration for vector-offset volumes. 82nd SEG annual international meeting, Expanded Abstracts.

Červený V. 2001. *Seismic Ray Theory*. Cambridge University Press.

Dash R., Spence G., Hyndman R., Grion S., Wang Y. and Ronen S. 2009. Wide-area imaging from OBS multiples. *Geophysics* **74**, Q41–Q47.

Fowler P.J., Du X. and Fletcher R.P. 2010. Coupled equations for reverse time migration in transversely isotropic media. *Geophysics* **75**, S11–S22.

Fowler P.J. and King R. 2011. Modeling and reverse time migration of orthorhombic pseudo-acoustic P-waves. 81st SEG annual international meeting, Expanded Abstracts.

Gray S.H. 2005. Gaussian beam migration of common-shot records. *Geophysics* **70**, S71–S77.

Gray S.H. 2013. Spatial sampling, migration aliasing, and migrated amplitudes. *Geophysics* **78**, S157–S164.

Gray S.H. and Bleistein N. 2009. True-amplitude Gaussian-beam migration. *Geophysics* **74**, S11–S23.

Grechka V., Zhang L. and Rector J.W. 2004. Shear waves in acoustic anisotropic media. *Geophysics* **69**, 576–582.

Hokstad K. 2000. Multicomponent Kirchhoff migration. *Geophysics* **65**, 861–873.

Hill N.R. 2001. Prestack Gaussian-beam depth migration. *Geophysics* **66**, 1240–1250.

Li X. 2008. An introduction to common offset vector trace gathering. *CSEG Recorder* **32**, 28–34.

Khalil A., Sun J., Zhang Y. and Poole G. 2013. RTM noise attenuation and image enhancement using time-shift gathers. 83rd SEG annual international meeting, Expanded Abstracts, 3789–3793.

Koren Z. and Ravve I. 2011. Full-azimuth subsurface angle domain wavefield decomposition and imaging Part I: Directional and reflection image gathers. *Geophysics* **76**, S1–S13.

Kuo J.T. and Dai T.F. 1984. Kirchhoff elastic wave migration for the case of noncoincident source and receiver. *Geophysics* **49**, 1223–1238.

Nowack R.L., Sen M.K. and Stoffa P.L. 2003. Gaussian beam migration for sparse common-shot and common-receiver data. 73rd SEG annual international meeting, *Expanded Abstracts*, 1114–1117.

Pšenčík I. and Farra V. 2005. First-order ray tracing for qP waves in inhomogeneous weakly anisotropic media. *Geophysics* **70**, D65–D75.

Ravve I. and Koren Z. 2011. Full-azimuth subsurface angle domain wavefield decomposition and imaging Part II: Local angle domain. *Geophysics* **76**, S51–S64.

Rosales D. and Rickett J. 2001. PS-wave polarity reversal in angle domain common-image gathers. 71st SEG annual international meeting, Expanded Abstracts, 1843–1846.

Stewart R.R., Gaiser J.E., Brown R.J. and Lawton D.C. 2002. Converted-wave seismic exploration: Methods. *Geophysics* **67**, 1348–1363.

Stewart R.R., Gaiser J.E., Brown R.J. and Lawton D.C. 2003. Converted-wave seismic exploration: Applications. *Geophysics* **68**, 40–57.

Sun R. and McMechan G.A. 2001. Scalar reverse-time depth migration of prestack elastic seismic data. *Geophysics* **66**, 1519–1527.

Thomsen L. 1986. Weak elastic anisotropy. *Geophysics* **51**, 1954–1966.

Trad D. 2009. Five-dimensional interpolation: Recovering from acquisition constraints. *Geophysics* **74**, V123–V132.

Tsvankin I. 2006. *Seismic Signatures and Analysis of Reflection Data in Anisotropic Media*, 2nd edn (first edition was published in 2001). Elsevier Science.

Ursin B. 2004. Tutorial: Parameter inversion and angle migration in anisotropic elastic media. *Geophysics* **69**, 1125–1142.

Vermeer G. 1990. Seismic wavefield sampling. *Society of Exploration Geophysicists*.

Vermeer G. 2012. 3-D Seismic Survey Design, 2nd edn. *Society of Exploration Geophysics, Geophysical References* **12**.

Vinje V., Roberts G. and Taylor R. 2008. Controlled beam migration: a versatile structural imaging tool. *First Break* **26**.

Zhang H., Zhang G. and Zhang Y. 2009. Removing S-wave noise in TTI reverse time migration. 79th SEG annual international meeting, Expanded Abstracts, 2849–2853.

Zhang Y., Zhang H. and Zhang G. 2011. A stable TTI reverse time migration and its implementation. *Geophysics* **76**, WA3–WA11.

Zhang H. and Zhang Y. 2011. Reverse time migration in vertical and tilted orthorhombic media 81st SEG annual international meeting, Expanded Abstracts.

Zhu T., Gray S.H. and Wang D. 2007. Prestack Gaussian-beam depth migration in anisotropic media. *Geophysics* **72**, S133–S138.

Zhu T. 2010. Dynamic raytracing in inhomogeneous anisotropic media. CSEG annual meeting, *Expanded Abstracts*, 1–4.